Volume 9
Number 17
7 September 2025
Pages 4499–4762

Sustainable Energy & Fuels

Interdisciplinary research for the development of sustainable energy technologies

rsc.li/sustainable-energy

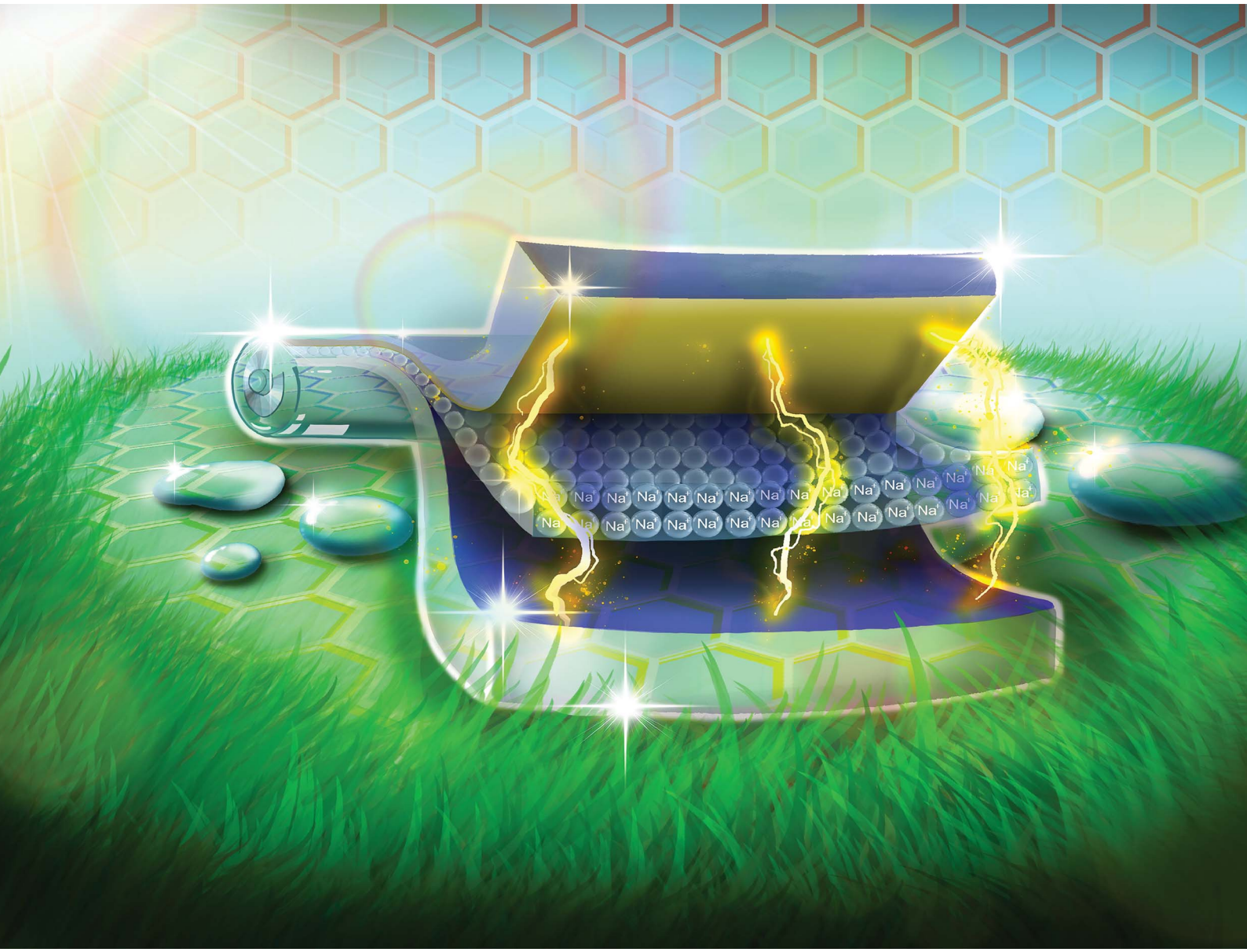

ISSN 2398-4902

ROYAL SOCIETY OF CHEMISTRY

PAPER

Maria K. Ramos and Aldo J. G. Zarbin
Eco-friendly, transparent, flexible and aqueous sodium-ion battery

Sustainable Energy & Fuels

ROYAL SOCIETY OF CHEMISTRY

PAPER

View Article Online
View Journal | View Issue

Cite this: *Sustainable Energy Fuels*, 2025, **9**, 4614

Eco-friendly, transparent, flexible and aqueous sodium-ion battery†

Maria K. Ramos and Aldo J. G. Zarbin *

This paper presents the integration of three advanced materials, combined through an innovative processing technique, to develop sustainable energy storage devices, specifically, eco-friendly, lightweight, transparent, and flexible sodium-ion batteries operating entirely in aqueous media. The final device configuration features a cathode composed of a cobalt hexacyanoferrate/carbon nanotube nanocomposite (CoHCF/CNTs), an anode based on a nanoarchitecture of reduced graphene oxide, molybdenum disulfide, and copper oxide nanoparticles (rGO/Cu_xO/MoS_2), and a polyvinyl alcohol/sodium chloride/boric acid hydrogel (PVA/NaCl/H_3BO_3) serving as both electrolyte and separator. Using either rigid (ITO/glass) or flexible (ITO/polyethylene terephthalate, PET) transparent electrodes, we fabricated transparent battery devices in rigid and flexible configurations. These were characterized using scanning electron microscopy and Raman spectroscopy, including *in operando* methods. The rigid device delivered a specific capacity of 73 mA h g^{-1} at 0.5 A g^{-1}, while the flexible configuration achieved at least 90 mA h g^{-1}. It also demonstrated excellent cycling stability, retaining 85% of its capacity after 2000 cycles at 2 A g^{-1}, with a coulombic efficiency exceeding 82%. The battery achieved an energy density of 43.1 W h kg^{-1} at a power density of 1.7 kW kg^{-1}. As a proof of concept, the device was used to power an LED by connecting multiple charged units.

Received 9th May 2025
Accepted 6th July 2025

DOI: 10.1039/d5se00665a

rsc.li/sustainable-energy

1. Introduction

Sodium-ion batteries (SIBs) have been considered promising candidates to replace the well-established lithium-ion batteries technology and improve energy storage devices' sustainability.[1] Currently, lithium-ion batteries (LIBs) are a widely used battery technology, responsible for the portable electronics revolution and offering superior energy density over other rechargeable systems.[2–5] However, there are many drawbacks associated to lithium-based devices: lithium resources are limited with poor distribution around the globe; the security issues associated to the growth of lithium dendrites during the charge/discharge cycles that can generate a short circuit due to the electrode connections; the high cost of materials and battery design; the low recyclability of discharged devices; and serious sustainable issues associated to the processes for lithium mining.[6–8] SIBs, otherwise, can reduce or substantially minimize these effects, once sodium is abundant and widely distributed, and its mining is usually carried out based on low-cost and cleaner processes.[7,8]

Another safety and environmental concern associated with LIBs refers to the volatile, toxic and flammable organic electrolytes employed in their manufacture. A green alternative consists of preparing aqueous rechargeable batteries, in which the organic solvents are replaced by aqueous electrolytes that present several advantages over the non-aqueous ones, as their inherent safety, cost-effectiveness, higher ionic conductivities, non-flammability, non-toxicity and environmental sustainability.[9–14] Otherwise, aqueous electrolytes present some drawbacks such as the narrow electrochemical window of water (due to the water electrolysis) and the specificity on the intercalation/deintercalation processes at the electrodes involving hydrated cations. So, replacing lithium by sodium in aqueous SIBs is not a trivial task and involves the development of strategies for preparing and processing new, safe, and cost-effective materials with higher intercalation capacity for hydrated sodium ions, at the narrow electrochemical window imposed by water, without compromising the environment.

In addition to replacing lithium and using aqueous electrolytes, there are other important technological demands in the development of novel metal-ion rechargeable batteries, especially in specific niches that involve multifunctionality, *i.e.*, batteries that beside perform their primary task (store and deliver energy), adding features like lightweight, flexibility, and transparency, for example.[15–17] Transparent or flexible batteries are critical emerging technologies responsible for the development of advanced devices. Transparent batteries are crucial to be integrated into photovoltaic devices, smart windows, displays, touch screens, and optical circuits, among others.[18,19]

Department of Chemistry, Federal University of Paraná (UFPR), Centro Politécnico, CP 19032, 81531-980, Curitiba, PR, Brazil. E-mail: aldozarbin@ufpr.br

† Electronic supplementary information (ESI) available. See DOI: https://doi.org/10.1039/d5se00665a

Flexible batteries could allow their integration into flexible and malleable devices, powering, for example, wearable technologies for e-textiles and healthcare.[20–23] However, there are enormous scientific and technological challenges to achieve transparent and flexible batteries, once (i) all battery components (materials for electrodes, electrolytes, separators, and current collectors) must be flexible and transparent while retaining mechanical strength and electrochemical functionality,[12,24] and (ii) the transparence and flexibility should remain after the integration of the individual component materials to originate the final device, which involves additional understanding on interfacial assembly of the components, as well as care on the significant space and volume required by batteries.[19,24,25] Materials for electrodes should be processed as thin films to guarantee optical transparency, in a connected and malleable way to guarantee flexibility, without losses in their electrochemical performance.[26] Aqueous electrolyte should be processed to avoid water evaporation and leaking, as well as electrolyte salt precipitation: the use of hydrogels has been considered a fruitful strategy, as they are stable, folded, safe, and can be easily integrated into the electrode materials.[27–31] Several strategies have been described to achieve all these requirements,[32–34] but to the best of our knowledge there are no reports in which all of those requirements are solved or presented together.

Our research group developed a very simple and elegant experimental route to both synthesize and process materials as thin, transparent and malleable films, based on the interface between two immiscible liquids.[35–38] Based on this so-called liquid/liquid interfacial route (LLIR), we described two multicomponent materials and demonstrated the potentiality of their use as electrodes in transparent batteries: a reduced graphene oxide/copper oxide nanoparticles/molybdenum disulfide nanoarchitected thin film nanocomposite ($rGO/Cu_xO/MoS_2$)[39] and a Prussian blue-analogue cobalt hexacyanoferrate/carbon nanotubes nanocomposite (CoHCF/CNTs).[18,40] The performance of each material individually, in a three-electrode half-cell configuration, demonstrated that $rGO/Cu_xO/MoS_2$ has high capacity to be used as anode while the CoHCF/CNTs present high potentiality to be used as a cathode, both in aqueous sodium-ion battery. Also, we demonstrated recently the preparation of a polyvinyl alcohol/sodium chloride/boric acid ($PVA/NaCl/H_3BO_3$) hydrogel, presenting stability, transparency, robustness, flexibility and ionic conductivity, which enables it to be used as an electrolyte in SIBs.[41] In this work, we present the integration of these three materials to build novel, sustainable and innovative energy storage devices: rigid or flexible, all solid-state, transparent, rechargeable, aqueous sodium-ion battery. To the best of our knowledge, this is the first report in which a flexible, transparent, aqueous and all-solid-state SIB device is reported.

2. Methodology

2.1. Chemicals

Toluene (99.9%, Sigma-Aldrich and 99%, Neon), chloroform (Neon, ethanol stabilized), sodium chloride (NaCl, Neon), potassium chloride (KCl, Neon), anhydrous acetonitrile (99.8%, Sigma-Aldrich), hydrochloric acid (HCl 35%, Panreac), graphite (90%, Graflake), potassium permanganate ($KMnO_4$, synth, 99%), sulfuric acid (H_2SO_4, 98%, Anhydrol), sodium nitrate ($NaNO_3$, Neon), hydrogen peroxide (H_2O_2, 30%, Vetec), copper(II) nitrate ($Cu(NO_3)_2$, Vetec), sodium borohydride ($NaBH_4$, 98%, Acros Organic), ammonium molybdate tetrahydrate ($(NH_4)_6Mo_7O_{24}\cdot 4H_2O$, Vetec), ammonium sulfide ($(NH_4)_2S$, 20% aqueous solution, Vetec), polyvinyl alcohol (PVA, degree of polymerization 86.5–89%, degree of hydrolysis 86.5–89.5%, Vetec), boric acid (H_3BO_3, Vetec), potassium ferricyanide ($K_3[Fe(CN)_6]$, Vetec), cobaltocene (Sigma-Aldrich), industrial and analytical argon (99% White Martins) were used as received. All solutions were prepared with ultrapure water using a Milli-Q purification system with $R = 18.2$ MΩ cm.

2.2. Cathode: cobalt hexacyanoferrate/carbon nanotubes (CoHCF/CNT) thin film

The cobalt hexacyanoferrate/carbon nanotubes (CoHCF/CNT) nanocomposite thin film was prepared as described in our previous report.[18,40,42] Summarizing, cobalt-filled multi-walled carbon nanotubes (CoCNTs) was prepared through the thermal decomposition of cobaltocene,[40] processed as thin films using the liquid-to-liquid interfacial route (LLIR)[43] and deposited over conductive and transparent substrates (ITO/glass or ITO/polyethylene terephthalate-PET). CoHCF was electrodeposited by cyclic voltammetry in an aqueous solution of 0.1 mmol L^{-1} $K_3[Fe(CN)_6]$ and 0.1 mol L^{-1} KCl at pH 4, in the potential range of −0.3 to 1.0 V *vs.* Ag/AgCl at 50 mV s^{-1} for 100 cycles. The CoCNTs film over transparent electrodes was used as the working electrode, a Pt wire as the counter electrode and Ag|AgCl (3.0 mol L^{-1}) as the reference electrode. The entire cycle to produce the CoHCF/CNTs is schematically summarized in Fig. 1a.

2.3. Anode: reduced graphene oxide, copper oxide nanoparticles and molybdenum disulfide ($rGO/Cu_xO/MoS_2$) nanocomposite thin film

Reduced graphene oxide, copper oxide nanoparticles and molybdenum disulfide nanocomposite ($rGO/Cu_xO/MoS_2$) thin films were prepared through a reaction in an interface between two immiscible liquids, as detailed in our previous work (Fig. 1b).[39] Summarizing, 8 mL of an aqueous solution of $Cu(NO_3)_2$ (0.3 mg mL^{-1}) was mixed with 4 mL of an aqueous dispersion of GO (0.15 mg mL^{-1}), 7 mL of a 0.14 mg mL^{-1} acetonitrile solution of MoS_2, and 11 mL of water in a 50 mL round-bottom flask, resulting in 30 mL of aqueous phase (totaling 0.02 mg mL^{-1} of GO, 0.08 mg mL^{-1} of $Cu(NO_3)_2$, and ~0.033 mg mL^{-1} of MoS_2, ratio 1 : 4 : 1.6). Then, 20 mL of toluene was added to originate the liquid/liquid interface, and this system was kept under magnetic stirring for two hours at 1500 rpm. After this time, 3 mL of an aqueous solution of $NaBH_4$ (40 mg mL^{-1}) was added with a syringe. After 30 minutes the stirring was stopped and a gray film was observed at the interface between the two liquids. The aqueous phase was

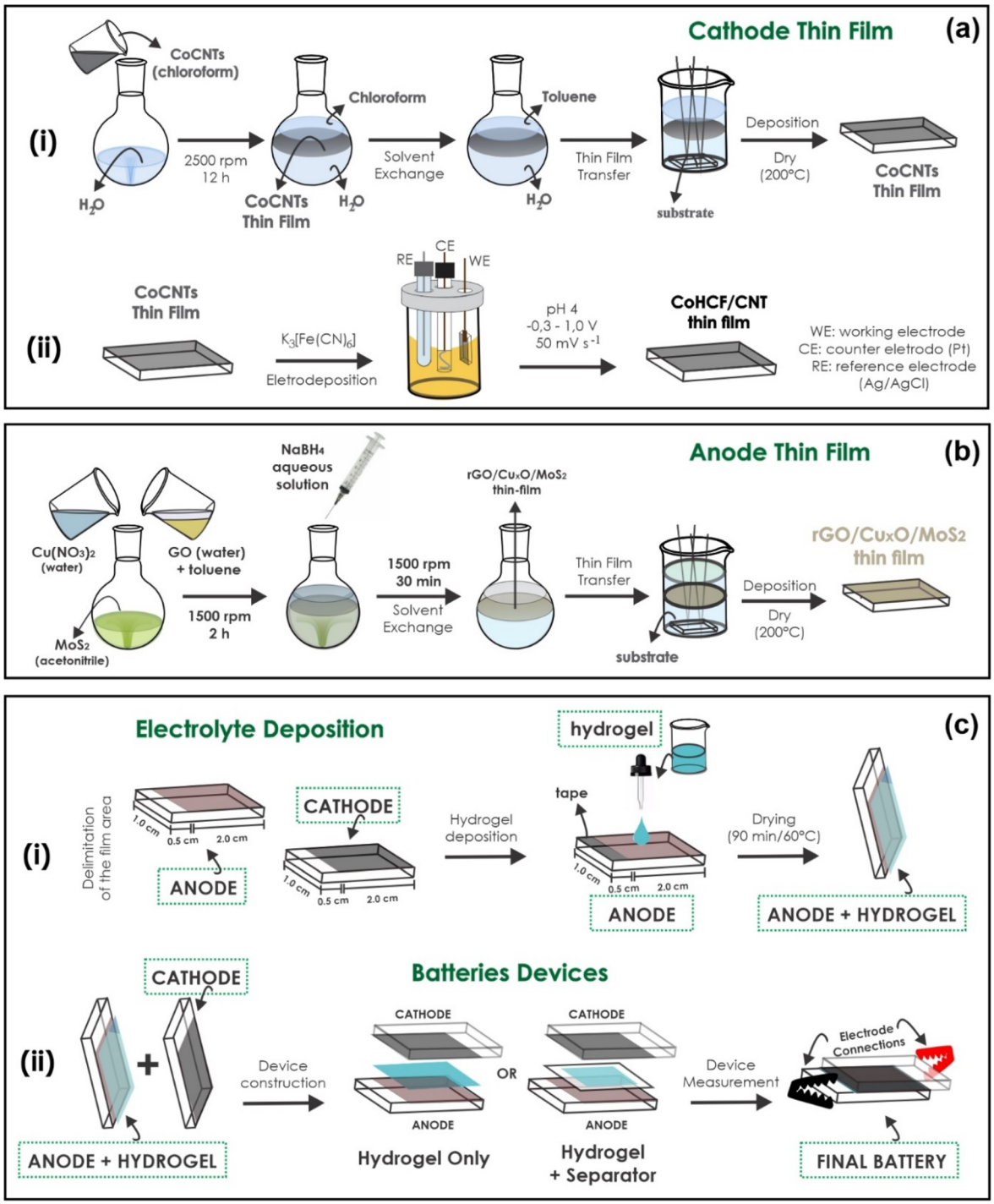

Fig. 1 (a) Schematic of CoCNT thin film formation and CoHCF electrodeposition using CoCNTs as precursor to obtain the CoHCF/CNTs nanocomposite; (b) schematic of the reaction to produce $rGO/Cu_xO/MoS_2$ thin film; (c) schematic of the hydrogel deposition on the anode electrode and on the battery device assembly.

exchanged for new aliquots of ultrapure water (removing the aqueous phase with a Pasteur pipette and adding a new portion of 30 mL of water) and the system was stirred for few minutes. This procedure was repeated 10 times, and it was done to remove excess of $NaBH_4$ and any remaining soluble impurities in the system. Next, the same procedure was twice performed with toluene. In the deposition process, the entire system (toluene/film/water) was transferred to a Becker containing the substrate (ITO/glass, for rigid devices, or ITO/PET, for flexible devices) immobilized in a stem, and by lifting the stem upwards, the films were deposited onto the substrates. The deposited film was dried at 200 °C for 2 h.

2.4. Electrolyte/separator: PVA/NaCl/H_3BO_3 hydrogel

PVA/NaCl/H_3BO_3 hydrogels were prepared by chemically cross-linking PVA with H_3BO_3 in the presence of NaCl.[41] Initially, 0.75 g of PVA was dissolved in 10 mL of deionized water under constant stirring (1000 rpm) and heated at 70 °C for 20 min. Subsequently, 0.03 g of H_3BO_3 and a known amount of 0.08 g of NaCl were dissolved in 1.5 mL of water. This mixture was then gradually added dropwise to the PVA solution. Immediately after, the resulting mixture was stirred and kept at 60 °C for 15 min, followed by another 10 min of continuous stirring without heating.

2.5. Assembly of the battery device

The devices were prepared using the CoHFC/CNTs as cathode, the rGO/Cu_xO/MoS_2 as anode and the PVA/NaCl/H_3BO_3 as both electrolyte and separator. Both the electrode films were deposited on a limited area of 2.0 × 1.0 cm^2 ITO/glass substrates. Over the anode film, 4 drops (0.2 mL) of the hydrogel dispersion freshly prepared were dropped and left to dry at ambient environment for 90 min, which is enough to get the gelation point. Afterwards, the second electrode (ITO/glass//CoHCF/CNT) was carefully deposited on top, forming a device ITO//rGO/Cu_xO/MoS_2//PVA/NaCl/H_3BO_3//CoHCF/CNT/ITO (Fig. 1c). The flexible devices were assembled following precisely the same methodology, but with the films previously deposited over ITO/PET electrodes instead of ITO/glass. Only for the experiments involving the stability analysis, a polydimethylsiloxane (PDMS) membrane approximately 0.2 mm thick with a window of 1.8 × 0.8 cm^2 was used as a spacer between the electrodes. The objective was to isolate the electrode area and not let the hydrogel dry completely during these long-time analyses.

2.6. Electrochemical measurements

Cyclic voltammetric measurements were performed in the potential window of 0.0 to 1.0 V (*vs.* Ag/AgCl) at scan rates ranging from 10 to 50 mV s^{-1}. Galvanostatic charge and discharge measurements were performed at 0.5, 0.75, 1, 2, 4 and 8 A g^{-1} (relative to the cathode mass).[18] The stability and coulombic efficiency of the device were evaluated after 2000 consecutive cycles at a current density of 2 A g^{-1}. The terminal devices were connected to an external battery to charge the cells, and a red LED with a nominal voltage of 3.0 V was used to demonstrate the battery working.

2.7. Characterizations

All materials obtained in all steps previously described were characterized by different techniques: (i) Raman spectroscopy: the analyses were performed on a Witec alpha 300R Confocal Raman microscope, with a lateral resolution of 200 nm, vertical resolution of 500 nm, using 633 nm laser with a resolution of 0.02 cm^{-1}; (ii) UV-Vis spectroscopy, performed in transmittance mode, using a Shimadzu UV-2450 spectrophotometer at wavelengths from 200 to 800 nm directly on the films deposited over the substrates or over the final device; (iii) scanning electron microscopy (SEM): the images were taken on a TESCAN Mira FEG-SEM equipment, using an in-beam detector (SE) and a backscattering detector (BSE), voltage of 10 kV at different magnifications; (iv) thickness analysis by atomic force microscopy (AFM): a Shimadzu SPM 9700 equipment was used in dynamic mode with a NanoWorld NCHR PointProbe silicon probe coated with aluminum on the detector side with a force constant of 42 N m^{-1} and resonance frequency of 320 kHz. For thickness analysis, a small region of the sample surface was cleaned with isopropanol to remove the film. The probe scanned the sample surface perpendicularly to the interface of the films and the substrate; (v) electrochemical measurements were performed in an AUTOLAB potentiostat, controlled by the GPES version 4.9 and NOVA 1.11 software; (vi) cross-section analysis: once fully dried, the hydrogel was detached from the current collector, bringing along the adhered cathode and anode thin films. This composite (hydrogel + thin film) was used for SEM and Raman analyses. Each spectrum was analyzed using Lorentzian fitting to precisely determine the position of each band.

3. Results and discussion

The strategy adopted to prepare the battery devices consists on the deposit the active materials of each electrode over transparent electrodes to be used as charge collector (ITO/glass for the rigid device and ITO/PET for the flexible one), followed by the controlled dropping of the hydrogel solution over one of the electrodes and waiting for the gelation point, for finally attach the other electrode in the opposite side. This way, the hydrogel acts as an electrolyte and electrode separator, reducing the number of materials necessary for the device production.

Fig. 2 presents the scanning electron microscopy (SEM) images of each component of the battery. A comprehensive physical and electrochemical characterization of these materials is available in our previous work.[39,41] The cathode (CoHCF/CNT) consists of multi-walled carbon nanotubes (MWCNTs) with their cavities filled by cobalt/cobalt oxide nanoparticles, in which the electrochemical reaction with an aqueous solution of $K_3[Fe(CN)_6]$/KCl yields the CoHCF. The final material is characterized by nanometric CoHCF cubic structures attached to the CNTs walls, as shown in Fig. 2a–d. The anode (rGO/Cu_xO/MoS_2) comprises graphene sheets with well-defined folds and edges, MoS_2 nanoplates, and a mixture of CuO and Cu_2O nanoparticles (generically represented here as Cu_xO nanoparticles), which exhibit cubic and undefined morphologies along with smaller nanoparticles (Fig. 2e–h). The electrolyte/separator consists of an interconnected network of H_3BO_3-reticulated PVA embedding some NaCl crystals (Fig. 2i–l).

We observed during the battery assembly a very effective contact between the electrolyte gel and both films of the cathode and anode, resulting in a strong adherence of the films on the gel surface, which was very useful to the characterization of the device structure, as well as to the performance of the device. After the device assembly and the full drying of the gel, it was possible to carefully detach the transparent collector (ITO/glass), and the films remained integrally adhered to the gel surface. The SEM images of the cross-sectional film/hydrogel/film are presented in Fig. 3. Initially observing the cathode

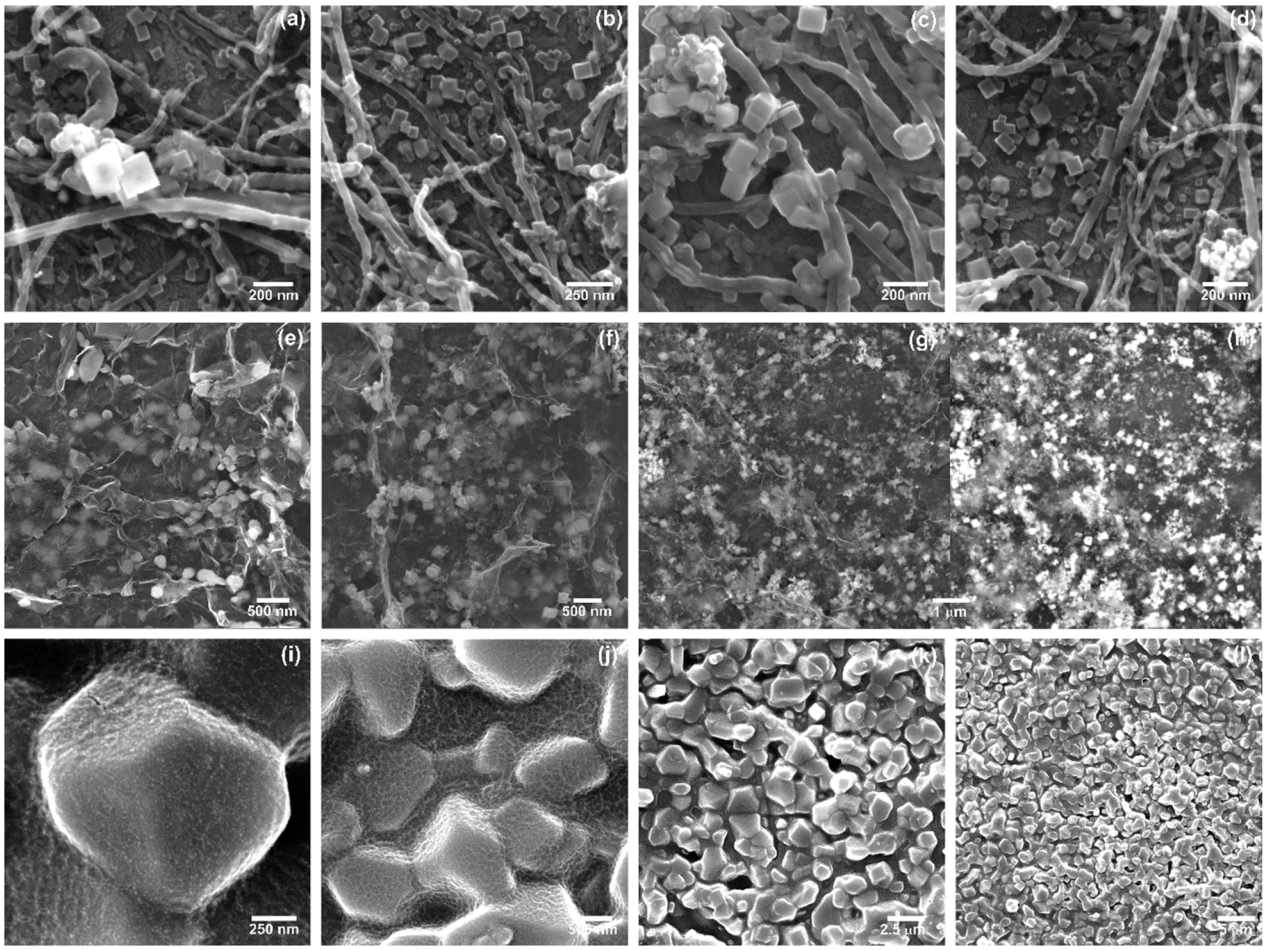

Fig. 2 Scanning electron microscopy images of the cathode thin film CoHCF/CNT (a–d); anode thin film rGO/Cu_xO/MoS_2 (e–h); and electrolyte/separator PVA/NaCl/H_3BO_3 (i–l).

side (Fig. 3a–d), it is seen this excellent adherence and improved contact between the film and the electrolyte. The film is significantly thinner than the electrolyte, in which well-defined carbon nanotubes decorated with the CoHCF can be observed (Fig. 3a–d). Fig. 3e–h show the opposite side, related to the interface of the hydrogel electrolyte with the anode film. The morphology of small graphene sheets and MoS_2 nanoflakes organized as a very thin film adhering to the hydrogel surface is detectable at the hydrogel/film interface. Overall, the images reveal a close and intimate contact between both electrode materials and the hydrogel, a critical factor contributing to the battery performance, which will be discussed in the following.

Thickness measurements of the cathode and anode films were obtained using atomic force microscopy (AFM), revealing that the rGO/Cu_xO/MoS_2 film has an average thickness of 67 nm, while the thickness of 110 nm was found for the CoHCF/CNT. Both films are very thin, mainly compared to the micrometric thickness of the electrolyte.

Energy dispersive X-ray spectroscopy (EDS) mapping was conducted on the cross-section of the device. A folded region of the hydrogel was selected for detailed analysis, with EDS mapping performed both on the inner side of the fold (Fig. 3i–n) and the top of the fold (Fig. 3o–t). The inner region, shown in Fig. 3i–n, corresponds to the cathode side in which the elemental maps highlight the presence of C, Co, Fe, and N – elements characteristic of the CoHCF structure. Additionally, the top of the folded area mapped in Fig. 3o–t shows a concentration of C, Cu, O, and Mo, which are key elements in the anode thin film (rGO/Cu_xO/MoS_2). The EDS analysis also revealed a uniform distribution of sodium throughout the hydrogel structure, consistent with the high NaCl content used in the hydrogel formulation.

The intimate contact between the films and the electrolyte hydrogel can also be measured by Raman spectroscopy. Fig. 4 shows the Raman spectra of the films before and after the device assembly, *i.e.*, as they were deposited over the ITO/glass before the contact with the hydrogel, and after the device was assembled and the ITO/glass was removed. The Raman spectrum of the hydrogel is presented in Fig. S1.† A summary of the main Raman bands observed in the spectra presented in Fig. 4 is provided in Tables S1 and S2.†

The spectra of the cathode (Fig. 4a) exhibit the characteristic bands of the carbon nanotubes: (i) the G band at approximately 1584 cm^{-1}, which corresponds to the E_{2g} vibrational mode

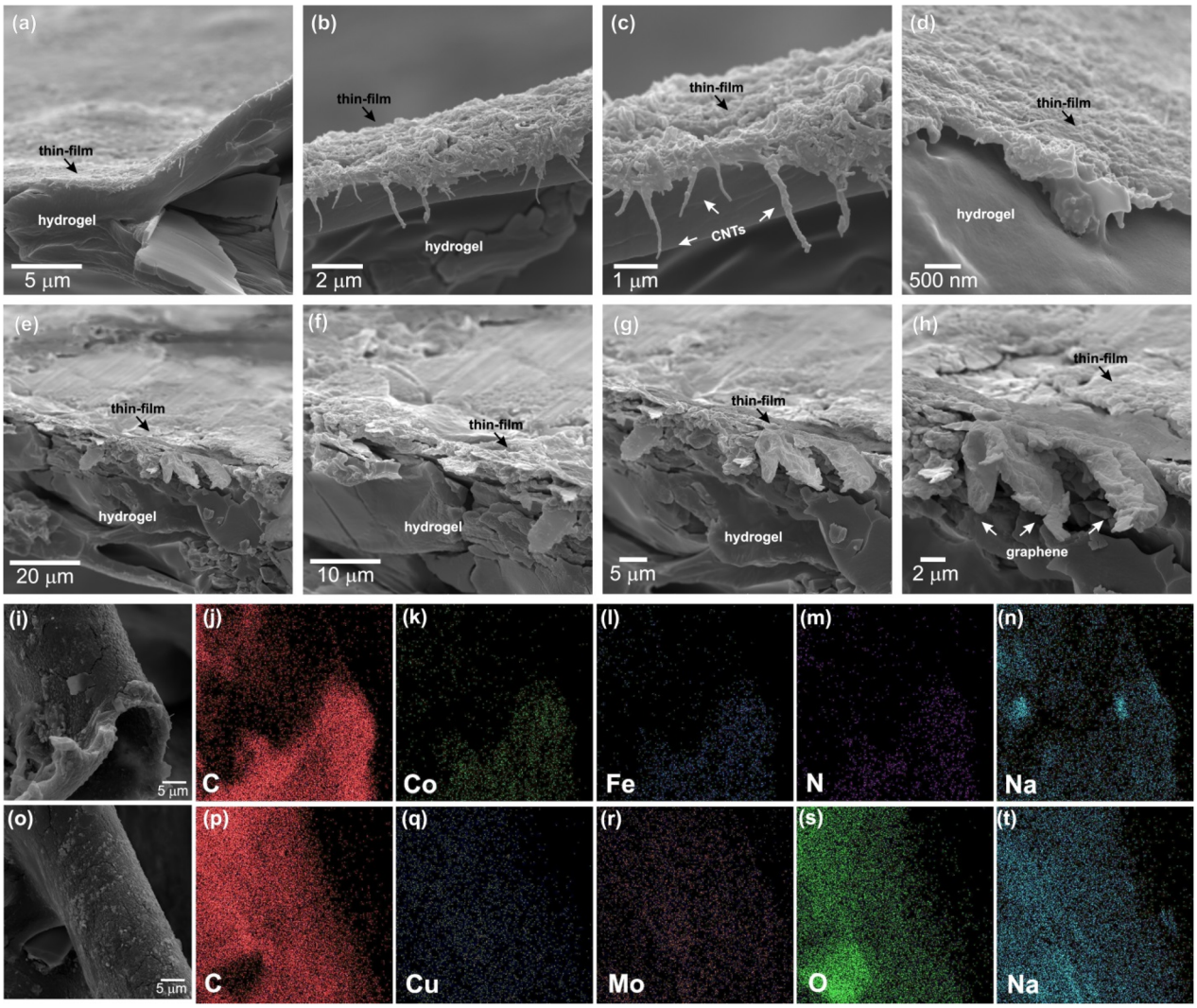

Fig. 3 Scanning electron microscopy cross-section images of the film/electrolyte/film device, showing the cathode/electrolyte interface (a–f) and the anode/electrolyte interface (g and h). Energy-dispersive spectroscopy mapping of the cathode/electrolyte (i–n) and anode/electrolyte (o–t) interfaces.

associated with the C–C stretching of graphene sheets; (ii) the D band at 1584 cm^{-1}, which arises from the symmetry break due to defects in the hexagonal graphene lattice; (iii) the D′ band at 1612 cm^{-1}, indicates defects in the sp^2 graphitic structure; (iv) the G′ (or 2D) band at 2664 cm^{-1} which is an overtone of the D band.[40,44] Also, the spectrum shows the typical CoHCF bands: (i) CN stretching from Fe^{II}–CN–Co^{II} chemical environment at 2089 cm^{-1}; (ii) CN stretching from Fe^{II}–CN–Co^{III} at 2121 cm^{-1}; (iii) CN stretching from Fe^{III}–CN–Co^{II} at 2151 cm^{-1}; (iv) 273 cm^{-1} due to the Fe–CN vibration.[40,45,46] Low intensity bands at 690 and 529 cm^{-1} can also be seen due to the presence of Co_3O_4 inside the CNTs structure. After the device assembly and in direct contact with the gel, some spectral changes can be seen (Fig. 4a and Table S1†): (i) related to the CNTs bands, an intensification of both the D and D′ bands and a redshift of the G band (from 1584 to 1581 cm^{-1}), which are indicative of a chemical interaction between the CNTs and the hydrogel, similar to a n-doping of CNTs by the hydrogel;[47,48] (ii) related to the CoHCF bands, a redshift on the most intense CN stretching mode, due to the CN at Fe^{III}–CN–Co^{II} chemical environment, from 2151 to 2147 cm^{-1}, indicating a perturbation of the hydrogel on the CoHCF structure.

The Raman spectrum of rGO/Cu_xO/MoS_2 anode (Fig. 4b) shows the typical graphene bands, similar to the ones previously described for CNTs (the G band at 1597 cm^{-1} and the D band at 1327 cm^{-1}) as well as the main bands associated to 2H-MoS_2: at 383 cm^{-1} and 408 cm^{-1}, referring to the E^1_{2g} and A_{1g} modes, respectively (in-plane and out-of-plane S–Mo–S vibrations);[49] an intense band at 455 cm^{-1} attributed to the second-order 2LA(M) mode, involving two longitudinal acoustic phonons at the M point of the Brillouin zone; and other low intensity bands arising from the resonance effect due to the coincidence between the excitation energy and an electronic transition of the MoS_2 at 179 cm^{-1} ($A_{1g}(M) - LA(M)$ mode), 570 cm^{-1} ($2 \times E_{1g}(\Gamma)$ mode), 598 cm^{-1} ($E_{2g}(M) + LA(M)$ mode), and 642 cm^{-1} ($A_{1g}(M) + LA(M)$ mode).[50–52] No bands due to the

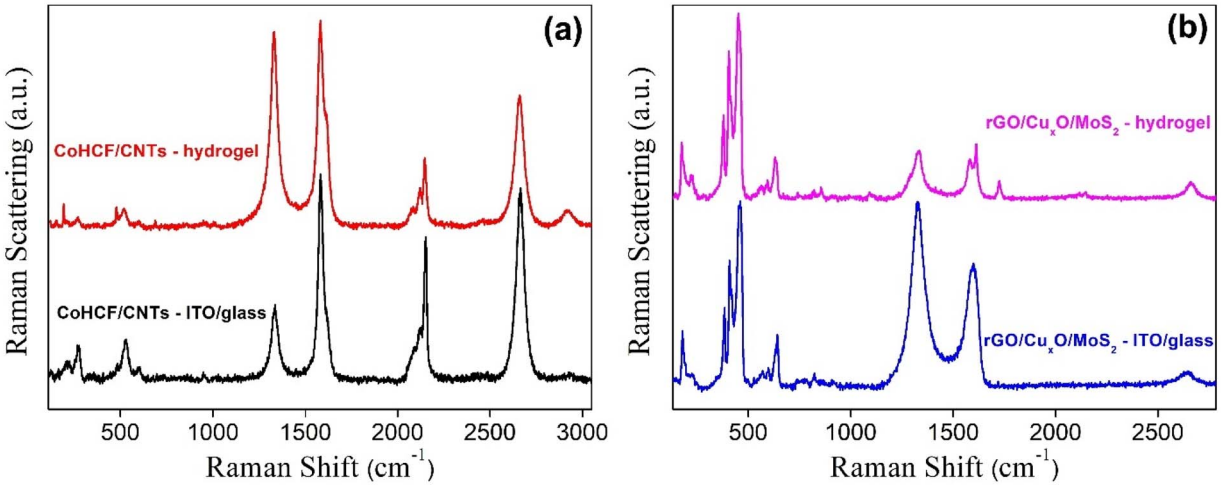

Fig. 4 (a) Raman spectra of the thin films of the cathode CoHCF/CNT (a) and the anode rGO/Cu_xO/MoS_2 (b) over ITO/glass and attached to the surface of the electrolyte hydrogel.

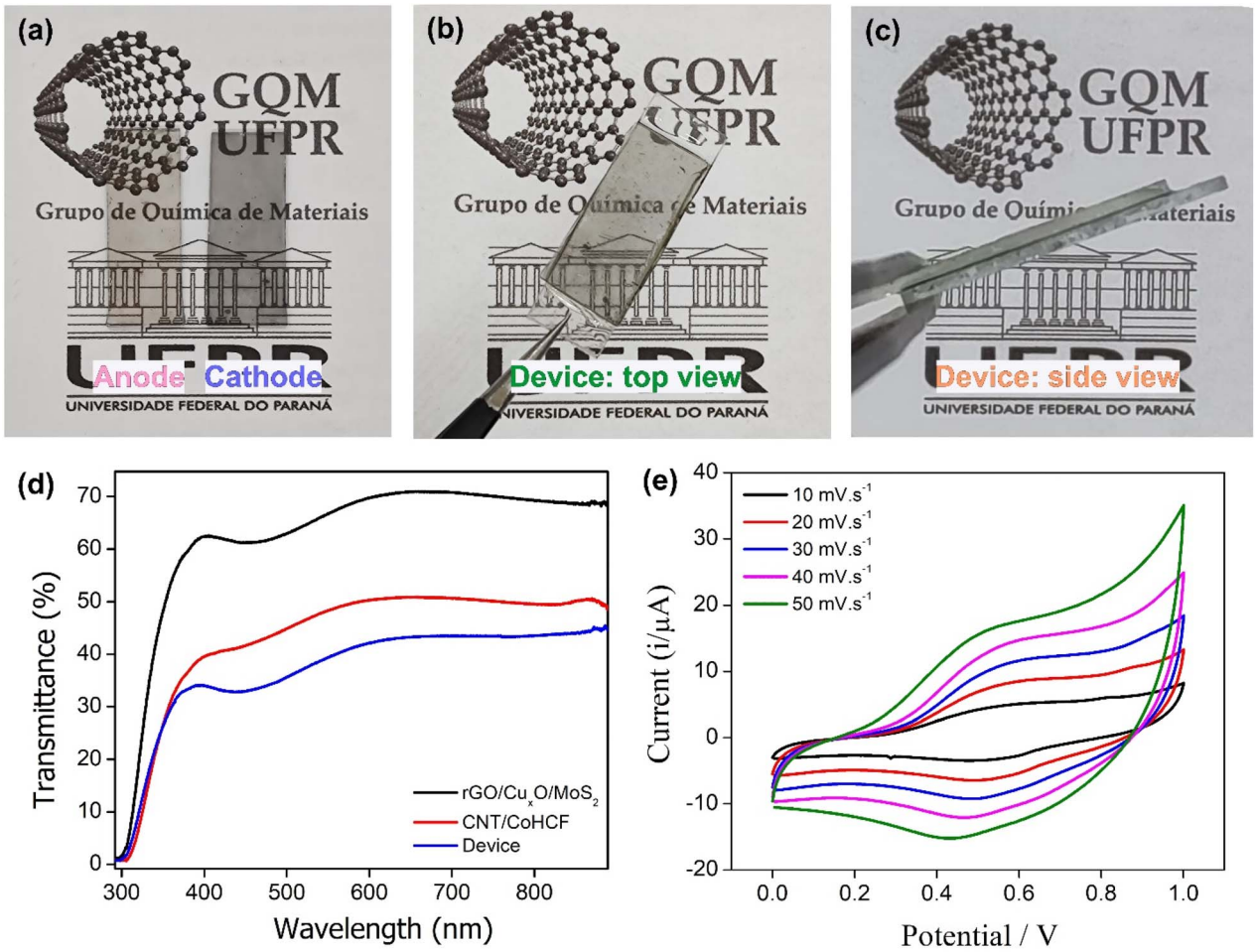

Fig. 5 Digital photographs of the anode (rGO/Cu_xO/MoS_2) and cathode (CoHCF/CNT) films deposited on ITO/glass electrode (a); digital photograph of the assembled battery device showing its transparency (b) and thickness (c); transmittance spectra of the cathode, anode and complete device films, all obtained on ITO/glass substrate (d); cyclic voltammetry of the battery device at scan rates varying from 10 to 50 mV s^{-1} (e).

Cu_xONPs were identified in the Raman spectra of the nanocomposite thin film, exactly because they are expected to be overlapped by the MoS_2 bands. It is noteworthy the changes in the Raman spectral profile of the film attached to the hydrogel surface: as observed for the cathode, the graphene G band are redshifted (from 1597 to 1591 cm^{-1}) and a well-defined D′ band appears at 1611 cm^{-1}, characterizing again the effective chemical interaction between the graphene and the hydrogel, in a n-doped like graphene by the hydrogel; a redshift in almost all MoS_2 related bands (from 179 to 176; from 383 to 377; from 408 to 406; from 455 to 451 from 570 to 564; from 598 to 594; from 642 to 633 cm^{-1}), evidencing again the perturbation of the MoS_2 by the hydrogel.

The SEM images presented and discussed in Fig. 3 and the Raman data presented and discussed in Fig. 4 strongly evidence the success of the engineering strategy adopted here to assemble the components to produce the battery device. The intimate contact between the components, the interface interaction, the absence of non-contacted regions, the adherence and chemical affinity between the components are crucial to guarantee good performance allied to transparency and flexibility.

Fig. 5a shows a digital image of the cathode and anode deposited over ITO/glass before the device assembly (in which their high transparency, homogeneity, and optical quality can be easily seen), and Fig. 5b and c show the final rigid device photographed at different angles. The assembled device maintains uniform transparency and a thickness of 2.0 mm (Fig. 5c), exclusively due to the glass substrate on which the active materials are deposited. Fig. 5d presents the transmittance spectra of the individual cathode and anode, and of the final assembled device. The transmittance values at 550 nm are 68%, 50%, and 39% for the anode, cathode, and assembled device, respectively.

The electrochemical response of the device was studied by cyclic voltammetry (CV) recorded at scan rates ranging from 10 to 50 mV s^{-1}, as shown in Fig. 5e. A broad redox process with $E_{1/2} \approx 0.55$ V is observed. This process occurs in the same potential region previously reported by our group for CoHCF in both a three-electrode cell[42] or in a non-solid-state device.[18] The CoHCF structure exists in its most reduced form as Na_2-$Co^{II}[Fe^{II}(CN)_6]$ at the potential range of 0.0 to 0.2 V, and changes to $NaCo^{III}[Fe^{II}(CN)_6]$ at potential between 0.2 and 0.7 V, compatible with the redox pair around $E_{1/2} \approx 0.55$ V, corresponding to the Co(II)/Co(III) redox couple.[53,54] Above 0.8 V, the most oxidized form, $Co^{III}[Fe^{III}(CN)_6]$, can be formed. In this study, this final redox process is not well-defined; however, a slight oxidation process around ~0.85 V is observed at lower scan rates, which may be associated with the formation of this highly oxidized structure.

Charge and discharge (CD) experiments were performed on the final device, and the results are presented in Fig. 6a and b (complete CD curves and only the discharge curves). The data show a strong correlation with the cyclic voltammograms,

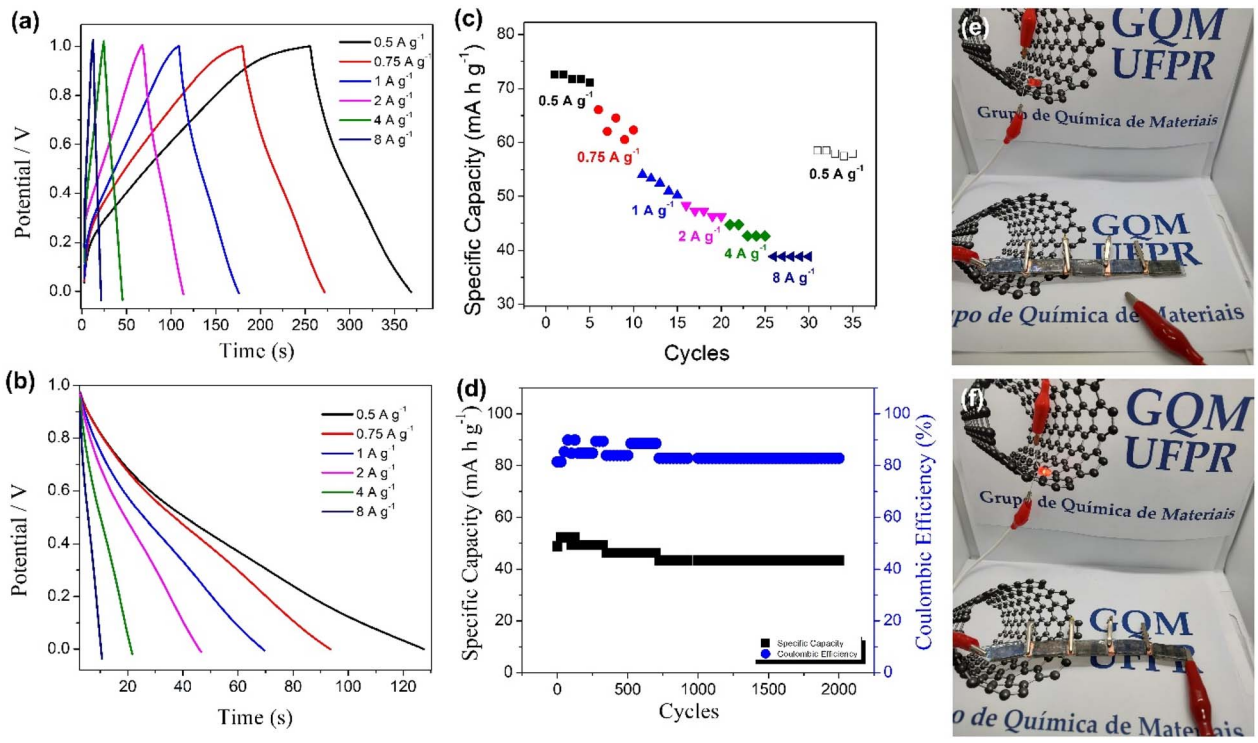

Fig. 6 Performance of the rigid transparent aqueous SIB device: charge/discharge profile (a) and discharge profile (b) as a function of time at different current densities (0.50, 0.75, 1.00, 2.00, 4.00, and 8.00 A g^{-1}); device performance at different current densities (specific capacity *vs.* number of cycles) (c); specific capacity (black) and coulombic efficiency (blue) of 2000 charge/discharge cycles of the device (d); digital photography of five charged devices connected in series at opened (e) and closed (f) circuit, lightening a 3.0 V LED.

exhibiting redox plateaus at $E_{1/2} \approx 0.5$ V (Fig. 6a and b) associated with the $Na_2Co^{II}[Fe^{II}(CN)_6]/NaCo^{III}[Fe^{II}(CN)_6]$ redox pair. Fig. 6b highlights the discharge time of the device, demonstrating a prolonged discharge even at high current densities. Fig. 6c illustrates the cycling performance of the device, in which the specific capacity is calculated at sequential CD processes starting at a low current density (0.5 A g^{-1}), increasing to higher current densities (8 A g^{-1}), and returning to the initial current density (0.5 A g^{-1}). The specific capacity (SC) was normalized to the cathode mass, reaching values of 73 mA h g^{-1} at 0.5 A g^{-1} and 48 mA h g^{-1} at 2 A g^{-1}. Even at a high current rate of 8 A g^{-1}, the device maintained a capacity of 38 mA h g^{-1}, showcasing its excellent performance under fast CD conditions. The device showed 80% capacity retention when restarted at 0.5 A g^{-1}.

The long-term stability of the device was also demonstrated (Fig. 6d), maintaining 85% of the SC after two thousand cycles at 2 A g^{-1}, and a coulombic efficiency (CE) above 82%. The CE below 100% indicates the occurrence of some side reactions stemming from design limitations such lack of full sealing and absence of artificial interfacial layers (AIL). Despite this, it is considered a very good performance, favored compared to the best metal-ion batteries in the literature. Finally, under the applied conditions, the rigid transparent aqueous SIB presented an energy density of 43.1 W h kg^{-1} to 1.7 kW kg^{-1}. To demonstrate the application of the device, Fig. 6e and f and Video S1 (ESI)† show five charged devices connected in series capable of lighting a 3.0 V LED.

In order to understand the role of each component during the device performance, a confocal Raman spectroelectrochemistry *in operando* analysis was performed, as illustrated in Fig. 7. Photographs of the setup employed to collect these data are shown in Fig. S2a and S2b.† The focus was adjusted crossing the glass and the ITO, directly to the thin film at the anode side of the device, and the spectra were acquired in a fixed region at different applied potentials, associated with the CV curve presented in Fig. 5 and detailed in Fig. S3.† A total of seven spectra were recorded: the first one with no applied potential, followed by spectra at applied potentials of 0.0, 0.5, 1.0, 0.5, and 0.0 V (in this order – as shown in Fig. S3†), and finally another spectrum without applied potential. The normalized spectra are shown in Fig. 7, detailed in different spectral regions. The full-range spectra (Fig. 7a), as well as zoomed-in at the regions between 25 to 300 cm^{-1} (Fig. 7b), 200 to 700 cm^{-1} (Fig. 7c) and 1000 to 1800 cm^{-1} (Fig. 7d) are included.

The most evident changes in the spectroscopic profile are related to the MoS_2 bands, evidencing its fundamental role of

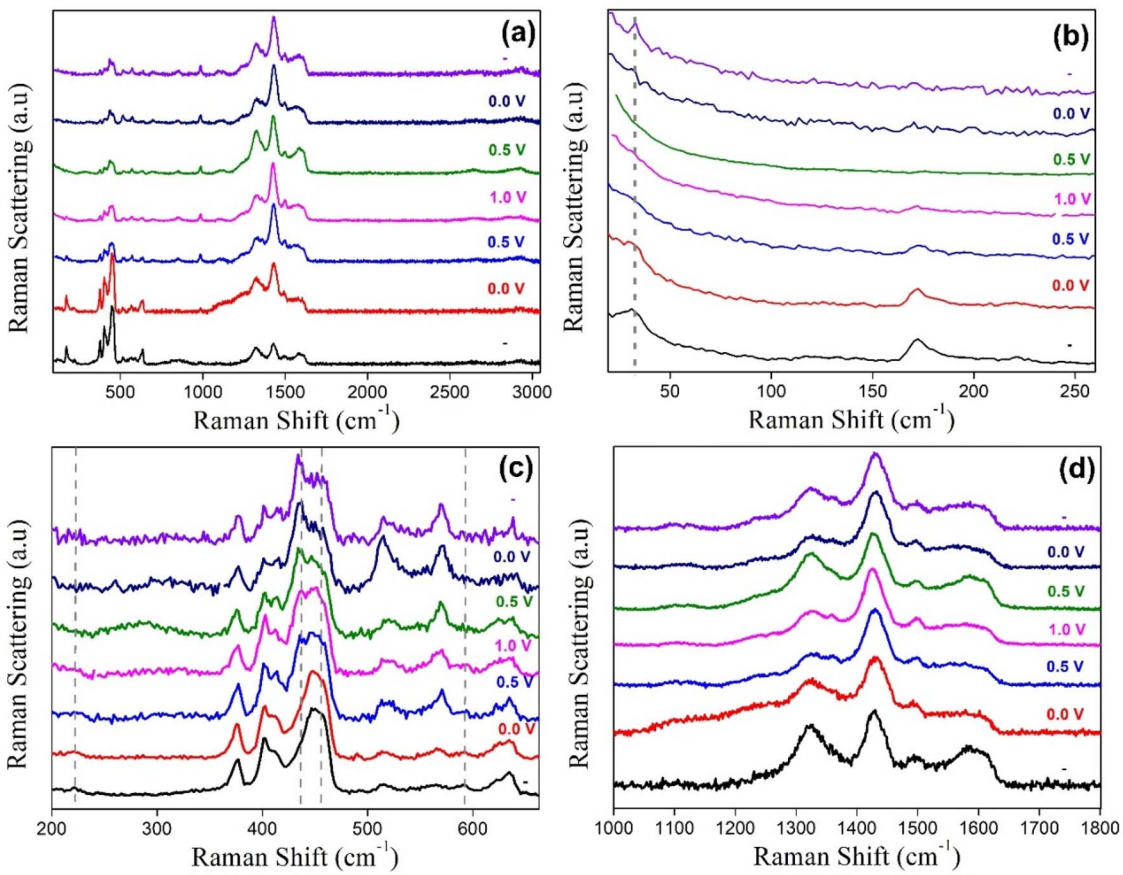

Fig. 7 Confocal Raman spectroelectrochemistry *in operando* data collected at different potentials (0.0, 0.5, 1.0, 0.5 and 0.0 V) using 633 nm laser. The sequence was from bottom (black curve) to top (purple curve) showing the full-range spectra (a) and the zoom at the regions between 25 to 300 cm^{-1} (b). 200 to 700 cm^{-1} (c) and 1000 to 1800 cm^{-1} (d).

this component during the charge/discharge process. During the oxidation, Na^+ migrates into the anode materials, and the Raman results in Fig. 7 evidence the intercalation into the MoS_2 structure. The low intensity E^2_{2g} mode at 30 cm^{-1} (Fig. 7b) is attributed to a phonon vibration characteristic of layered materials involving interlayer atomic movement. This band disappears during cation intercalation (E = 0.5 V) and only reappears when the potential returns to 0.0 V, after complete deintercalation. During intercalation, cations occupy the space between the MoS_2 layers, disrupting this vibration and causing the associated band to disappear. Once deintercalation occurs, the interlayer spacing is restored, allowing the vibration – and thus the band – to reappear. A similar trend is observed for the LA(M) band at 226 cm^{-1} and the A_{1g}(M) + LA(M) mode at 642 cm^{-1}. The most significant change occurs in the 2LA(M) mode (Fig. 7c), in which the original band at 450 cm^{-1} splits into two distinct bands at approximately 435 and 455 cm^{-1} upon applying 0.5 V. During the reduction process, following deintercalation at 0.5 V, the intensity ratio of these two bands shifts, further indicating structural modifications.

All the bands discussed before result from processes involving coupling with the longitudinal acoustic mode, LA(M).[55] The LA(M) mode at 226 cm^{-1} is considered a disorder-induced longitudinal acoustic mode located at the M point of the Brillouin zone.[52] Similar to what is observed in nanocrystalline graphite and SiC, this mode arises due to phonon scattering from structural defects and the presence of a limited number of atomic layers.[51] Therefore, the disappearance of this band during the oxidation process may be attributed to the intercalation of cations into defective sites within the MoS_2 structure. This behavior aligns with the well-known fact that MoS_2 present pseudocapacitive properties, exhibiting both intercalation and surface adsorption processes, particularly at defect sites.[36,39] The difficulty in detecting this band after the intercalation process may be due to the cations becoming trapped within defect regions of the MoS_2 structure, preventing their exit and, consequently, the reappearance of the band—unlike the reversible behavior observed in modes associated with intercalation. Similar effects should be expected to understand the splitting of the band at 450 cm^{-1} upon Na^+ intercalation. This band (2LA(M) mode) is an overtone of the 226 cm^{-1} band (LA(M) mode) and is significantly enhanced under resonance conditions (as employed here) due to coupling with electronic transitions associated with excitonic states.[52]

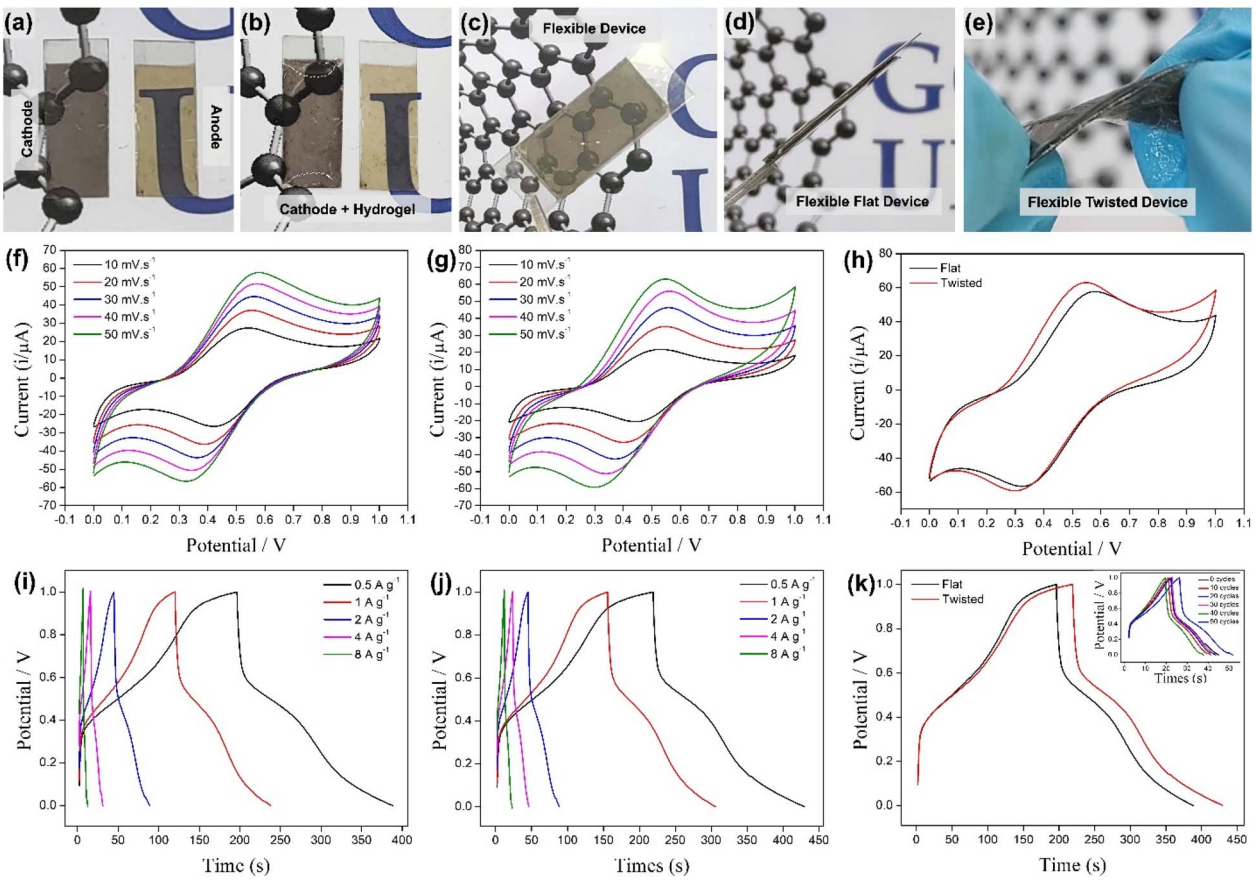

Fig. 8 Digital photographs of the anode (rGO/Cu_xO/MoS_2) and cathode (CoHCF/CNT) films deposited on PET/ITO electrodes (a); digital photograph of the anode with hydrogel applied (b); digital photograph of the assembled flexible battery device (c); digital photographs of the device in flat (d) and twisted (e) configurations; cyclic voltammetry curves of the flexible battery device at scan rates ranging from 10 to 50 mV s^{-1} in flat (f) and twisted (g) configurations; a comparison of the charge/discharge curves at 50 mV s^{-1} of the device at flat and twisted configuration (h); galvanostatic charge/discharge curves at various current densities in flat (i) and twisted (j) configurations; comparison of charge/discharge performance at 0.5 A g^{-1}, with an inset showing 50 CD cycles at 4 A g^{-1} in the twisted configuration (k).

Although the exact nature of the band splitting is difficult to define, it is supposed to be associated to the intercalation and deintercalation of Na^+ ions within the MoS_2 layers at 0.5 V during the oxidation/reduction processes. These changes may also be influenced by pseudocapacitive behavior in the MoS_2 structure, particularly involving defect sites, similar to what has been described for the LA(M) mode. The structural changes detected by the *in situ* Raman experiments, mainly related to bands associated to defects in MoS_2, could explain the CE below 100%, as some ions intercalate into the structure but do not leave in the reverse process, affecting stability.

Fig. 7d shows the region of the D sand G bands of the rGO (with the hydrogel band at 1430 cm^{-1} between them). Small changes in the G band (shift position and broadening of the band) demonstrate that the rGO also has an effective role, as a capacitive material.

The Raman spectroelectrochemical data obtained for these films are unprecedented and provide strong evidence of intercalation/deintercalation and adsorption processes occurring within the MoS_2 structure and rGO. This confirms the active role of these materials in the tricomponent rGO/Cu_xO/MoS_2 film. In contrast, the Cu_xO-related bands are either not clearly visible or are overlapped by the strong resonant bands of MoS_2, making it difficult to analyses the electrochemical behavior of the Cu_xO component.

Finally, a flexible and transparent device can also be prepared through the same methodology, depositing the active electrode materials over flexible and transparent electrodes, as ITO/PET (Fig. 8). Although this is not the best choice, due to the brittle nature of ITO, it is enough to demonstrate the viability and potential of the technique to prepare this multitask device. Fig. 8a–c displays digital photographs of the cathode and anode deposited on ITO/PET substrates at different stages: prior to device assembly (Fig. 8a), following hydrogel deposition on cathode substrate (Fig. 8b), and after complete assembly (Fig. 8c). These images clearly demonstrate the transparency, uniformity, and optical quality of the films. Fig. 8d and e show the fully assembled device from flat and twisted perspectives, respectively. The final flexible device had an approximate thickness of 0.6 mm and could be easily bent in both directions, emphasizing its mechanical flexibility.

CV and CD experiments were performed on both the flat and twisted configurations of the flexible device, with the results shown in Fig. 8f–k. CV curves recorded at scan rates from 10 to 50 mV s^{-1} for the flat (Fig. 8f) and twisted (Fig. 8g) configuration closely resemble those of the rigid devices, displaying redox plateaus at $E_{1/2} \approx 0.5$ V, corresponding to the Na_2-$Co^{II}[Fe^{II}(CN)_6]$/$NaCo^{III}[Fe^{II}(CN)_6]$ redox pair. A comparison of the CV curve recorded at 50 mV s^{-1} in both flat and twisted configuration is shown in Fig. 8h, in which a similar profile can be seen, with slightly higher current observed in the twisted configuration.

CD curves obtained at 0.5 to 8 A g^{-1} for the flat (Fig. 8i) and twisted (Fig. 8j) configuration closely resemble those of the rigid devices (a comparison of the CD curves at 0.5 A g^{-1} is presented Fig. 8k). The CD measurements (Fig. 8i–k) demonstrated very significant results: (i) the plateau in the discharge profile in the flexible device is much more defined than in the rigid devices (Fig. 8i–k); (ii) the plateau at $E_{1/2} \approx 0.5$ V related to the $Co^{(II)}$/$Co^{(III)}$ pair is also observed for these curves; (iii) a higher SC

Table 1 Aqueous battery devices found in the literature comparable to the ones described in this work, highlighting the electrode, the electrolyte, the specific capacity or specific capacitance (SC) in mA h g^{-1} or Faraday (F), the current (*I*) in A g^{-1}, the energy density (*E*) in W h kg^{-1}, the power (*P*) that was measured in W kg^{-1}, the stability (Stab. in %), the number of cycles and the coulombic efficiency (CE) (in %)

Battery	Cathode	Anode	Electrolyte	SC	*I*	*E*	*P*	Stab.	Cycles	EC	Ref.
This work	CoHCF	rGO/Cu_xO/MoS_2	PVA/NaCl (hydrogel)	73	0.5	43	1.7	85	2.000	82	This work
	CuHCF	Carbon/ polypyrrole	KCl (aq)	54	17 C	45	10 C	83	1.00	99.9	58
	CuHCF	Carbon/polyaniline	$Ca(NO_3)_2$ (aq)	70	10 C	70	250	95	1.000	—	59
	PB/crumple graphene	Crumple graphene	KCl (aq)	25	0.25	—	—	—	35	100	60
PBA	NiHCF/CoHCF	Carbon	Na_2SO_4 (aq)	50	—	42.5	21	89	5.000	—	61
	CoHCF	Graphene	Na_2SO_4 (aq)	55	10	34.4	2.5	—	—	—	62
	CNT/CoHCF	Zn	Na^+/Zn^{2+} (aq)	93	0.1	107	7.9	—	—	—	63
	CNT/CoHCF	Co/Co_3O_4@C	NaCl (aq)	32	0.05	19.2	1.4	100	2.000	99	18
	MoS_2	Zn	PVA/$Zn(CF_3SO_3)_2$ (hydrogel)	215	0.1	161.3	—	—	—	—	64
	MoS_2	Zn	PVDF/$Zn(CF_3SO_3)_2$ (hydrogel)	150	0.1	—	—	97	600	—	65
	MoS_2	rGO	Li_2SO_4 (aq)	1150	0.1	360	82	93	600	—	66
MoS_2	MoS_2/graphene	Zn	PVA/$Zn(CF_3SO_3)_2$ (hydrogel)	285	0.05	158	—	88	1.800	—	67
	MoS_2/Pedot	Zn	PVA/$ZnSO_4$ (hydrogel)	162	5	185	—	93	300	—	68
	MoS_2/Pani/rGO	rGO	Li_2SO_4 (aq)	432 F	8	56	0.45	94	30.000	—	69
	N-doped rGO	N-doped rGO	PVA/LiCl (hydrogel)	—	—	23 m	—	84	20.000	85	70
Graphene	rGO/Fe/MnO_2	rGO/carbon	PVA/KOH (hydrogel)	48 F	0.5	59	0.75	92	8.000	—	71
	PTCDA/rGO	PTCDA/rGO	Li_2SO_4 (aq)	163	1	19.7	45	91	5.000		72
	CuO/TiO_2	Carbon	KOH (aq)	553 F	1	34	800	96	10.000	—	73
Cu_xO	Cu/CuO/Cu_2O	Cabon	KOH (aq)	1480 F	1	9.7	750	76	—	—	74
	CuO	rGO	KOH (aq)	1300 F	1	152	4.3	78	—	—	75

value of 90 mA h g^{-1} at 0.5 A g^{-1} for the flexible electrode *vs.* 73 mA h g^{-1} at 0.5 A g^{-1} for the rigid electrode was obtained; (iv) higher SC values (102 mA h g^{-1} at 0.5 A g^{-1}) were obtained when the electrode was twisted. These results can probably be attributed to a more effective contact between the flexible electrode and the gel electrolyte, resulting in a higher current and a more significant SC, in a similar way as previously demonstrated in the literature.[56,57] Furthermore, when the electrodes are twisted, there is an accommodation of the gel with the electrodes, leading to more intimate contact and an enhanced electrochemical response. To evaluate the effect of the flexibility, the device underwent 50 torsion cycles with CD measurements at 4 A g^{-1} taken every 10 cycles, as shown in the inset of Fig. 8k. The discharge time varied slightly (±5 s), indicating reasonable stability, especially considering the use of PET/ITO, which is not ideal for torsion tests.

Finally, a comparison with similar devices reported in the literature is provided in Table 1. This table compiles data from reports on fully assembled aqueous batteries/supercapacitor devices that feature cathodes based on Prussian Blue (PB) or analogues (PBA) and anodes composed of graphene and/or MoS_2 and/or Cu_xO and/or nanocomposites between them. The comparison includes key parameters such as electrolyte composition, specific capacity or capacitance (SC), energy density (*E*), power (*P*), stability, and coulombic efficiency (CE) values. As observed, the reports on complete aqueous battery cells are relatively scarce, and studies on aqueous transparent batteries are even more limited. Finding reports on aqueous, transparent, and flexible batteries was even more challenging, particularly considering that our search was not restricted to electrodes produced as thin films like ours (which range from 60 to 110 nm in thickness). These factors, combined with the high electrochemical capacity and excellent stability demonstrated in this study, position our battery as competitive with similar materials reported in the literature. This highlights how LLIR played a key role in differentiating our work. The synthesis routes used here to fabricate thin films with one, two, or multiple components—while maintaining simplicity, scalability, and outstanding properties—are not easily found in the literature.

4. Conclusion

The findings presented in this paper represent a meaningful advance in the development of sustainable, transparent, and flexible aqueous sodium-ion batteries. By integrating three previously reported materials, each with independently demonstrated promise for energy storage, we achieved efficient performance in both rigid and flexible device formats. Specifically, the good performance of the devices reported here rest on three core innovations: (i) the specific composition of the electrodes materials, in which bi- or three-component materials were nanoarchitected in way that the synergism was maximized; (ii) the fabrication of thin electrode films using the liquid–liquid interfacial method, enabling better control, uniformity and facility to transfer and assembly in the choose configuration; and (iii) the use of a novel self-sustainable hydrogel system that simultaneously serves as both electrolyte and separator. This hydrogel not only simplified assembly and eliminated leakage and gas formation, which are common challenges in aqueous systems, but also allowed closer electrode contact, improving ion transport and cell stability, and simplifying the assembly process.

The resulting devices deliver robust electrochemical performance while maintaining safety, low cost, and environmental compatibility, relying on water as the solvent and sodium as the charge carrier, both abundant and non-toxic. Moreover, the minimal use of active materials supports the development of lightweight, high-efficiency, and scalable energy storage systems aligned with the future devices needing transparency and flexibility.

As final considerations, it is important to emphasize that the development of transparent and flexible energy storage devices still faces key challenges across several performance factors, including transparency, lightweight design, areal capacity, flexibility, cycle life, and cost, each demanding specific solution strategies and still offering room for improvement. Thicker electrodes and higher material loading can reduce light transmittance and increase device weight. So, nanostructured, ultrathin, or mesh-like electrodes and optimized geometries such as grid patterns are key strategies to maintain optical transparency. Regarding areal capacity, thinner electrodes enhance surface-limited kinetics by promoting sodium-ion insertion near the surface, reducing bulk diffusion limitations. Achieving both high transparency and storage capacity requires careful material selection and synergistic integration. It was demonstrated that the strategies adopted in this work were highly efficient on this purpose.

In which concerns flexibility, the cycle life of thin or nanostructured electrodes may suffer from mechanical degradation or side reactions, which can be mitigated through improved interfacial adhesion and the use of stable low-strain materials, as also demonstrated here. Finally, flexibility is often limited by brittle materials, like ITO. The search for ITO-free flexible conductive networks and strain-absorbing architectures, enhancing mechanical durability, are currently being performed in our laboratory, as strategies to move forward to even more efficient, robust and durable devices.

Data availability

The data supporting the findings of this study are available within the article and its ESI.†

Author contributions

Maria K. Ramos: conceptualization, visualization, methodology, formal analysis, writing – original draft, writing – review & editing; Aldo J. G. Zarbin: conceptualization, funding acquisition, methodology, project administration, resources, supervision, validation, writing – review & editing.

Conflicts of interest

There are no conflicts to declare.

Acknowledgements

The authors acknowledge the financial support of CAPES, CNPq, INCT-Nanocarbon and INCT-NanoVida. M. K. R. is thankful to INCT-NanoVida for the fellowship.

References

1 L. Zhao, T. Zhang, W. Li, T. Li, L. Zhang, X. Zhang and Z. Wang, *Engineering*, 2023, **24**, 172–183.
2 L. David, R. Bhandavat and G. Singh, *ACS Nano*, 2014, **8**, 1759–1770.
3 J. Su, Y. Pei, Z. Yang and X. Wang, *RSC Adv.*, 2014, **4**, 43183–43188.
4 B. Wang, E. H. Ang, Y. Yang, Y. Zhang, M. Ye, Q. Liu and C. C. Li, *Chem.–Eur. J.*, 2021, **27**, 512–536.
5 J.-Y. Hwang, S.-T. Myung and Y.-K. Sun, *Adv. Funct. Mater.*, 2018, **28**, 1802938.
6 X. Jiang, Y. Chen, X. Meng, W. Cao, C. Liu, Q. Huang, N. Naik, V. Murugadoss, M. Huang and Z. Guo, *Carbon*, 2022, **191**, 448–470.
7 K. Amit, *Wired on Energy*, 2018, vol. 9, pp. 1–15.
8 C. Vaalma, D. Buchholz, M. Weil and S. Passerini, *Nat. Rev. Mater.*, 2018, **3**, 18013.
9 J. Y. Hwang, S. T. Myung and Y. K. Sun, *Chem. Soc. Rev.*, 2017, **46**, 3529–3614.
10 J. Liu, C. Xu, Z. Chen, S. Ni and Z. X. Shen, *Green Energy Environ.*, 2018, **3**, 20–41.
11 D. Chao, W. Zhou, F. Xie, C. Ye, H. Li, M. Jaroniec and S.-Z. Qiao, *Sci. Adv.*, 2020, **6**, eaba4098.
12 N. Alias and A. A. Mohamad, *J. Power Sources*, 2015, **274**, 237–251.
13 J. Xie, H. Zhang, Q. Liu, X. Liu and X. Lu, *Mater. Today Adv.*, 2020, **8**, 100100.
14 Q. Zhang, Z. Wang, S. Zhang, T. Zhou, J. Mao and Z. Guo, *Cathode Materials for Potassium-Ion Batteries: Current Status and Perspective*, Springer Singapore, 2018, vol. 1.
15 L. A. Wehner, N. Mittal, T. Liu and M. Niederberger, *ACS Cent. Sci.*, 2021, **7**, 231–244.
16 Z. Guo, Y. Zhao, Y. Ding, X. Dong, L. Chen, J. Cao, C. Wang, Y. Xia, H. Peng and Y. Wang, *Chem*, 2017, **3**, 348–362.
17 L. Zhao and Z. Qu, *J. Energy Chem.*, 2022, **71**, 108–128.
18 S. Husmann, M. K. Ramos and A. J. G. Zarbin, *Electrochim. Acta*, 2022, **422**, 140548.
19 O. Kwon, H. J. Hwang, Y. Ji, O. S. Jeon, J. P. Kim, C. Lee and Y. G. Shul, *Sci. Rep.*, 2019, **9**, 1–9.
20 M. Nasreldin, S. de Mulatier, R. Delattre, M. Ramuz and T. Djenizian, *Adv. Mater. Technol.*, 2020, **5**, 1–21.
21 X. Fan, B. Liu, J. Ding, Y. Deng, X. Han, W. Hu and C. Zhong, *Batteries Supercaps*, 2020, **3**, 1262–1274.
22 H. Yang, H. Fang, W. Wang, D. Zhang, J. Zhu, K. Chen, Y. Sun, P. Wang, Q. Zhou, C. Qi, B. Wang and M. Wu, *J. Power Sources*, 2024, **602**, 234350.
23 T. Huang, X. Yang, J. Xiao, H. Gao, Y. Wang, H. Liu and G. Wang, *J. Mater. Chem. A*, 2024, **12**, 13672–13681.
24 Z. Liu, J. Zhang, J. Liu, Y. Long, L. Fang, Q. Wang and T. Liu, *J. Mater. Chem. A*, 2020, **8**, 6219–6228.
25 Y. Yang, S. Jeong, L. Hu, H. Wu, S. W. Lee and Y. Cui, *Proc. Natl. Acad. Sci. U. S. A.*, 2011, **108**, 13013–13018.
26 M. J. Mirshojaeian Hosseini and R. A. Nawrocki, *Micromachines*, 2021, **12**, 1–19.
27 Z. Wang, H. Li, Z. Tang, Z. Liu, Z. Ruan, L. Ma, Q. Yang, D. Wang and C. Zhi, *Adv. Funct. Mater.*, 2018, **28**, 1–30.
28 N. Sun, H. Sun, D. Tan, Q. Guo, Z. Zhang, Z. Tao, C. Fang, J. Bu, J. Huang and C. Jiang, *Chem. Eng. J.*, 2023, **469**, 143997.
29 P. Bocchetta, D. Frattini, S. Ghosh, A. M. V. Mohan, Y. Kumar and Y. Kwon, *Materials*, 2020, **13**, 1–35.
30 H. Zhang, T. Xia, R. Chen, L. Zhang, X. Wang, H. Ma, Y. Chai, Z. Ren, J. Ji, X. Ma, M. Wu and M. Xue, *Small*, 2024, **21**, 1–9.
31 Z. Yang, Q. Zhang, T. Wu, Q. Li, J. Shi, J. Gan, S. Xiang, H. Wang, C. Hu, Y. Tang and H. Wang, *Angew. Chem.*, 2024, **63**, 1–9.
32 M. Yang, J. Luo, X. Guo, J. Chen, Y. Cao and W. Chen, *Batteries*, 2022, **8**, 1–23.
33 H. Ren, J. Liang, Q. Liu, Y. Wei and W. Wu, *Adv. Sci.*, 2025, **12**, 1–11.
34 H. Ren, X. Du, J. Liang and W. Wu, *J. Mater. Chem. A*, 2025, **13**, 12009–12038.
35 M. K. Ramos and A. J. G. Zarbin, *Appl. Surf. Sci.*, 2020, **515**, 146000.
36 A. Schmidt, M. K. Ramos, C. M. Ferreira, B. A. Braz and A. J. G. Zarbin, *Electrochim. Acta*, 2021, **387**, 1–12.
37 A. Schmidt, M. K. Ramos, C. S. Pinto, A. F. Pereira, V. H. R. Souza and A. J. G. Zarbin, *Electrochem. Commun.*, 2022, **134**, 107183.
38 C. M. Ferreira, M. K. Ramos and A. J. G. Zarbin, *Eur. J. Inorg. Chem.*, 2021, **2021**, 3373–3384.
39 M. K. Ramos, G. Martins, L. H. Marcolino-Junior, M. F. Bergamini, M. M. Oliveira and A. J. G. Zarbin, *Mater. Horiz.*, 2023, **10**, 5521–5537.
40 S. Husmann and A. J. G. Zarbin, *Chem.–Eur. J.*, 2016, **22**, 6643–6653.
41 R. Assis, M. Ramos and A. Zarbin, *J. Braz. Chem. Soc.*, 2024, **35**, 1–12.
42 S. Husmann and A. J. G. Zarbin, *Electrochim. Acta*, 2018, **283**, 1339–1350.
43 A. J. G. Zarbin, *Mater. Horiz.*, 2021, **8**, 1409–1432.
44 C. M. Pharr and P. R. Griffiths, *Anal. Chem.*, 1997, **69**, 4673–4679.
45 O. Calixto-Lozada, J. Vazquez-Samperio, E. Córdoba-Tuta, E. Reguera and P. Acevedo-Peña, *Solid State Sci.*, 2021, **116**, 106603.
46 R. Mažeikiene, G. Niaura and A. Malinauskas, *J. Electroanal. Chem.*, 2014, **719**, 60–71.
47 H. Terrones, R. Lv, M. Terrones and M. S. Dresselhaus, *Rep. Prog. Phys.*, 2012, **75**, 062501.
48 A. Forment-Aliaga, R. T. Weitz, A. S. Sagar, E. J. H. Lee, M. Konuma, M. Burghard and K. Kern, *Small*, 2008, **4**, 1671–1675.

49 A. Chakraborti, A. S. Patel, P. K. Kanaujia, P. Nath, G. V. Prakash and D. Sanyal, *Phys. Lett. A*, 2016, **380**, 4057–4061.
50 S. G. Drapcho, J. Kim, X. Hong, C. Jin, S. Shi, S. Tongay, J. Wu and F. Wang, *Phys. Rev. B: Condens. Matter Mater. Phys.*, 2017, **95**, 1–7.
51 J. E. Samaniego-Benitez, R. Mendoza-Cruz, L. Bazán-Díaz, A. Garcia-Garcia, M. J. Arellano-Jimenez, J. F. Perez-Robles, G. Plascencia-Villa, J. J. Velázquez-Salazar, E. Ortega, S. E. Favela-Camacho and M. José-Yacamán, *J. Mater. Sci.*, 2020, **55**, 12203–12213.
52 É. Blanco, P. Afanasiev, G. Berhault, D. Uzio and S. Loridant, *C. R. Chim.*, 2016, **19**, 1310–1314.
53 R. O. Lezna, R. Romagnoli, N. R. De Tacconi and K. Rajeshwar, *J. Phys. Chem. B*, 2002, **106**, 3612–3621.
54 N. R. De Tacconi, K. Rajeshwar and R. O. Lezna, *J. Electroanal. Chem.*, 2006, **587**, 42–55.
55 A. M. Stacy and D. T. Hodul, *J. Phys. Chem. Solids*, 1985, **46**, 405–409.
56 Z. Liu, D. Wang, Z. Tang, G. Liang, Q. Yang, H. Li, L. Ma, F. Mo and C. Zhi, *Energy Storage Mater.*, 2019, **23**, 636–645.
57 Z. Wang, F. Mo, L. Ma, Q. Yang, G. Liang, Z. Liu, H. Li, N. Li, H. Zhang and C. Zhi, *ACS Appl. Mater. Interfaces*, 2018, **10**, 44527–44534.
58 M. Pasta, C. D. Wessells, R. A. Huggins and Y. Cui, *Nat. Commun.*, 2012, **3**, 1149.
59 M. Adil, A. Sarkar, A. Roy, M. R. Panda, A. Nagendra and S. Mitra, *ACS Appl. Mater. Interfaces*, 2020, **12**, 11489–11503.
60 V. H. N. Martins, M. M. Silva, M. K. Ramos, M. H. Verdan, E. G. C. Neiva, A. J. G. Zarbin and V. H. R. Souza, *Nanoscale*, 2025, **17**, 11353–11365.
61 J. G. Wang, Z. Zhang, X. Zhang, X. Yin, X. Li, X. Liu, F. Kang and B. Wei, *Nano Energy*, 2017, **39**, 647–653.
62 F. Zhao, Y. Wang, X. Xu, Y. Liu, R. Song, G. Lu and Y. Li, *ACS Appl. Mater. Interfaces*, 2014, **6**, 11007–11012.
63 D. Zhang, Z. Yang, J. Zhang, H. Mao, J. Yang and Y. Qian, *J. Power Sources*, 2018, **399**, 1–7.
64 S. Li, Y. Liu, X. Zhao, K. Cui, Q. Shen, P. Li, X. Qu and L. Jiao, *Angew. Chem.*, 2021, **133**, 20448–20455.
65 Z. Sheng, P. Qi, Y. Lu, G. Liu, M. Chen, X. Gan, Y. Qin, K. Hao and Y. Tang, *ACS Appl. Mater. Interfaces*, 2021, **13**, 34495–34506.
66 Z. Xiao, L. Sheng, L. Jiang, Y. Zhao, M. Jiang, X. Zhang, M. Zhang, J. Shi, Y. Lin and Z. Fan, *Chem. Eng. J.*, 2021, **408**, 127269.
67 S. Li, Y. Liu, X. Zhao, Q. Shen, W. Zhao, Q. Tan, N. Zhang, P. Li, L. Jiao and X. Qu, *Adv. Mater.*, 2021, **33**, 1–9.
68 S. Li, C. Huang, L. Gao, Q. Shen, P. Li, X. Qu, L. Jiao and Y. Liu, *Angew. Chem., Int. Ed.*, 2022, **61**, 202211478.
69 J. Chao, L. Yang, H. Zhang, J. Liu, R. Hu and M. Zhu, *J. Power Sources*, 2020, **450**, 227680.
70 Q. Liu, J. Zhou, C. Song, X. Li, Z. Wang, J. Yang, J. Cheng, H. Li and B. Wang, *Energy Storage Mater.*, 2020, **24**, 495–503.
71 J. Tang, P. Yuan, C. Cai, Y. Fu and X. Ma, *Adv. Energy Mater.*, 2016, **6**, 1600813.
72 L. Wang, X. Ye, Y. Zhu, H. Jiang, J. Xia, Z. Yue, Z. Wan, C. Jia and X. Yao, *Electrochim. Acta*, 2020, **340**, 135804.
73 M. Z. U. Shah, M. Sajjad, H. Hou, S. ur Rahman, A. Mahmood, U. Aziz and A. Shah, *J. Energy Storage*, 2022, **55**, 105492.
74 M. Mamizadeh, S. M. Masoudpanah, M. S. Bafghi and M. P. Dabir, *J. Energy Storage*, 2023, **63**, 106989.
75 A. L. Jadhav, S. L. Jadhav, B. K. Mandlekar and A. V. Kadam, *Mater. Chem. Phys.*, 2023, **310**, 128494.